



# Facile preparation of well-dispersed ZnO/cyclized polyacrylonitrile nanocomposites with highly enhanced visible-light photocatalytic activity

Qingzhi Luo, Xiaolian Yang, Xiaoxiao Zhao, Desong Wang\*, Rong Yin, Xueyan Li, Jing An

School of Sciences, Hebei University of Science and Technology, Shijiazhuang 050018, People's Republic of China

## ARTICLE INFO

### Article history:

Received 9 August 2016

Received in revised form 9 November 2016

Accepted 19 November 2016

Available online 21 November 2016

### Keywords:

Nanocomposite

ZnO

Polyacrylonitrile

Calcination in nitrogen atmosphere

Visible light photocatalytic activity

## ABSTRACT

Well-dispersed zinc oxide/cyclized polyacrylonitrile (ZnO/CPAN) nanocomposites were prepared by a facile in-situ precipitation method. The mixture solution of dimethyl sulfoxide containing zinc nitrate and polyacrylonitrile (PAN) was added dropwise into ammonia water under vigorous magnetic stirring. Accompanied by the precipitation of PAN in water, zinc hydroxide were simultaneously formed via in-situ reaction of zinc nitrate with hydroxyl ions, leading to the uniform dispersion of zinc hydroxide nanoparticles in the precursor of ZnO/PAN nanocomposites. Then ZnO/CPAN nanocomposites were prepared by calcining the obtained precursor at 250 °C in nitrogen atmosphere via cyclization/dehydrogenation reaction of PAN and decomposition reaction of Zn(OH)<sub>2</sub>. The as-prepared ZnO/CPAN nanocomposites were characterized by XRD, SEM, XPS, UV-vis DRS, PL, etc. Results show that CPAN molecules in ZnO/CPAN nanocomposites significantly decrease the mean size of ZnO nanocrystals, increase the quantity of oxygen defects in ZnO particles, improve the absorbance of ZnO in the whole wavelength range especially in the visible-light range, and obviously reduce the recombination probability of photo-generated electron/hole pairs. The photocatalytic activity of ZnO/CPAN nanocomposites was evaluated by photodegradation of methyl orange (MO) solution under visible light irradiation. Experiment results reveal that the apparent rate constant k of MO photodegradation under visible light irradiation photocatalyzed by ZnO/CPAN ( $0.361\text{ h}^{-1}$ ) is 1.28, 5.84 and 25.8 times of that by AgBr ( $0.282\text{ h}^{-1}$ ), Ag<sub>3</sub>PO<sub>4</sub> ( $0.0618\text{ h}^{-1}$ ) or g-C<sub>3</sub>N<sub>4</sub> ( $0.0140\text{ h}^{-1}$ ), respectively, meaning that ZnO/CPAN exhibits much higher visible-light photocatalytic activity than these typical visible-light photocatalysts. The visible-light photocatalytic mechanism has been discussed.

© 2016 Elsevier B.V. All rights reserved.

## 1. Introduction

Semiconductor-based heterogeneous photocatalysis has drawn a great deal of attention in the fields of environmental contaminants treatment, clean hydrogen energy production, and photoelectrochemical conversion [1–4]. Among the various semiconductors, ZnO is one of the most promising and most widely researched photocatalysts because of its excellent oxidation capacity, good physical and chemical stability, non-toxicity, abundant availability, and low cost [5–7]. However, the large band gap of 3.37 eV makes ZnO be activated only by high-energy UV light irradiation (<370 nm) and leads to its low-efficiency utilization of solar energy. Furthermore, the high recombination rate of the photogen-

erated electron–hole pairs in ZnO seriously reduces its quantum efficiency and photocatalytic activity [8,9]. Thereby, numerous efforts have been devoted to extending the light-responsive range and enhancing the visible-light photocatalytic activity of ZnO, including morphology and composition controlling [10–12], metal depositing [13–15], nonmetal elemental doping [16,17], dye sensitization [18] and semiconductor coupling [19–21]. Hybridizing ZnO with carbonaceous materials containing spatially extended π-bonding structure is another effective strategy to solve the above-mentioned problems, because the π-conjugated carbonaceous materials possess unique electrical and optical properties, such as high mobility of charge carriers, strong absorption in visible light region, and excellent environmental stability [22,23]. For example, ZnO nanoparticles coated with graphite-like C<sub>3</sub>N<sub>4</sub> [24–26] and graphene [27,28] could exhibit obviously enhanced visible-light photocatalytic activity. Unfortunately, because of the van der Waals interactions between g-C<sub>3</sub>N<sub>4</sub> or graphene sheets, it

\* Corresponding author.

E-mail addresses: [dswang06@126.com](mailto:dswang06@126.com), [wangdesong@hebust.edu.cn](mailto:wangdesong@hebust.edu.cn) (D. Wang).

is difficult to obtain monolayer  $g\text{-C}_3\text{N}_4$  or graphene and to control the thickness and distribution state of  $g\text{-C}_3\text{N}_4$  or graphene sheets on the surface of ZnO, which is unfavorable for the improvement of the photocatalytic activity of ZnO. Zhang et al. [29] reported that polyaniline monolayer hybridized ZnO was prepared by the chemisorption method, and showed improved photocatalytic activity for the degradation of the methylene blue both under ultraviolet and visible light irradiation. Qiu et al. [30] used conjugated poly-(fluorene-co-thiophene) as a photosensitizer of ZnO for visible-light photocatalytic removal of phenol, rhodamine B, and methyl orange. These  $\pi$ -conjugated carbonaceous materials can remarkably extend the absorbance of ZnO to visible light region and improve the separation efficiency of photogenerated electrons and holes.

Polyacrylonitrile (PAN) is one of the most common polymers. When PAN is heated at the temperature range of 200–300 °C, the cyclization and dehydrogenation reaction can easily occur and a conjugated PAN derivative (CPAN) with cyclized ladder structure is formed, which has been successfully used for the modification of other semiconductor materials [31]. Similarly, when the ZnO/PAN nanocomposites are heated at the same temperature range in nitrogen atmosphere, PAN in the nanocomposites can be changed into CPAN, which can enhance visible-light photocatalytic activity of ZnO like polyaniline and polythiopene. Simultaneously,  $\text{H}_2$  produced from the dehydrogenation of PAN can despoil the oxygen atom of ZnO in the nanocomposites to form defects, which is possibly advantageous to visible-light photocatalytic activity of ZnO. Therefore, it is reasonable to infer that the ZnO/CPAN nanocomposites can exhibit excellent visible-light photocatalytic performances.

In this work, a facile method has been developed for preparing well-dispersed ZnO/CPAN nanocomposite as an efficient visible-light photocatalyst using polyacrylonitrile (PAN) and zinc nitrate hexahydrate ( $\text{Zn}(\text{NO}_3)_2 \cdot 6\text{H}_2\text{O}$ ) as main materials. Firstly,  $\text{Zn}(\text{NO}_3)_2 \cdot 6\text{H}_2\text{O}$  and PAN were dissolved into dimethyl sulfoxide. Then the obtained mixture solution was added dropwise into ammonia water under vigorous magnetic stirring. Accompanied by the precipitation of PAN in water, zinc hydroxide were simultaneously formed via in-situ reaction of zinc nitrate with hydroxyl ions, leading to the uniform dispersion of zinc hydroxide nanoparticles in the precursor of ZnO/PAN nanocomposites. Finally, ZnO/CPAN nanocomposites were prepared by calcining the nanocomposite precursor at 250 °C for 60 min in nitrogen atmosphere via cyclization/dehydrogenation reaction of PAN and decomposition reaction of  $\text{Zn}(\text{OH})_2$ . The as-prepared nanocomposite was characterized by X-ray diffraction (XRD), high-resolution transmission electron microscopy (HRTEM), Fourier transform infrared spectra (FT-IR), X-ray photoelectron spectroscopy (XPS), and so on. The visible-light photocatalytic activity and stability were evaluated by the photodegradation of methyl orange (MO) and sodium phenolate under visible light irradiation.

## 2. Experimental

### 2.1. Materials

Zinc nitrate hexahydrate was purchased from Aladdin Industrial Corporation. Dimethyl sulfoxide (DMSO), methyl orange and sodium phenolate were obtained from Tianjin Yongda Chemical Reagent Co, Ltd, China. All these reagents were of analytically pure grade and used without further purification. Potassium persulfate (Tianjin Damao Reagents Company, China) was purified by recrystallization from water. PAN was prepared using a traditional deposition polymerization with acrylonitrile (Zhengzhou Piney Chemical Reagent Co., Ltd., China, purified by the vacuum



**Scheme 1.** Idealized formation procedure of ZnO/CPAN nanocomposites.

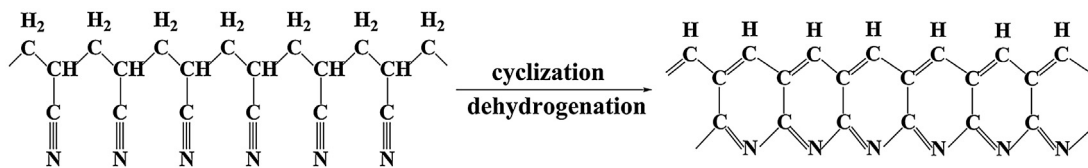
distillation) as the monomer. Deionized water was used in all the experiments.

### 2.2. Photocatalyst preparation

The idealized formation procedure of ZnO/CPAN nanocomposites is shown in **Scheme 1**. A typical procedure for preparing ZnO/CPAN nanocomposites is described as follows. Firstly, 0.500 g of PAN and 1.833 g  $\text{Zn}(\text{NO}_3)_2 \cdot 6\text{H}_2\text{O}$  were dissolved in 25 mL of DMSO. Then the obtained solution was added dropwise into ammonia water (0.17%, 250 mL) under vigorous magnetic stirring for 30 min. After another 30 min stirring and subsequently standing for 12 h, the resultant mixture was filtered, washed with deionized water for 3 times, and dried at 60 °C for 4 h to obtain the precursor of ZnO/PAN nanocomposite. Finally, ZnO/CPAN nanocomposite was prepared by calcining the ZnO/PAN precursor in a tube furnace at 250 °C for 60 min in nitrogen atmosphere via cyclization/dehydrogenation of PAN (shown in **Scheme 2**) and decomposition of  $\text{Zn}(\text{OH})_2$ . The nitrogen atmosphere for the calcination process is conducive to dehydrogenation and formation of conjugated structure of PAN and can avoid the oxidization of PAN molecular chain. Following the above-described procedure, a series of ZnO/CPAN nanocomposites were prepared and designated as ZnO/CPAN (x:y), where x:y means the mass ratio of ZnO to PAN. Pure ZnO nanoparticles were prepared without the presence of PAN under the same conditions. For comparison, several typical visible-light photocatalysts such as AgBr,  $\text{Ag}_3\text{PO}_4$  and  $g\text{-C}_3\text{N}_4$  were prepared according to the literature [32–34].

### 2.3. Photocatalyst characterization

XRD patterns of the samples were characterized in the region of  $2\theta$  from 5° to 100° by a Rigaku D/MAX-2500 diffractometer with Cu K $\alpha$  radiation ( $\lambda = 0.15406 \text{ nm}$ ) operated at 40 kV and 150 mA. The morphology of the samples was recorded by scanning electron microscopy (SEM, HITACHI S-4800) with an accelerating voltage of 10 kV. High-resolution transmission electron microscopy (HRTEM) measurements were examined on a G2 F20 electron microscopy instrument (Tecnai Co., Holland) using an accelerating voltage of 200 kV. Fourier transform infrared spectra (FT-IR) of the samples were performed on a Prestige-21 spectrometer (Shimadzu Co., Japan) in the range of 400–4000  $\text{cm}^{-1}$  with KBr as the reference sample. The measurements were performed in the transmission mode with spectroscopic grade KBr pellets for all the powders. UV-vis diffuse reflectance spectra (UV-vis DRS) were performed by a Shimadzu-2550 Scan UV-vis system equipped with an integrating sphere attachment over a range of 200–800 nm with  $\text{BaSO}_4$  as a reference. X-ray photoelectron spectroscopy (XPS) analysis were investigated by a PHI 5000C ESCA



**Scheme 2.** Cyclization and dehydrogenation reaction of PAN during calcination process in nitrogen atmosphere.

System with Al K $\alpha$  radiation ( $h\nu = 1486.6$  eV). The X-ray anode was run at 250 W, and the high voltage was kept at 15.0 kV with a detection angle of 54°. Photoluminescence (PL) emission spectra were recorded on a Fluorescence spectrophotometer (FS5-TCSPC Research Spectrofluorometer, Edinburgh Instruments Ltd, United Kingdom) with 150 W ozone free Xe source. The excitation wavelength was 250 nm. Electrochemical impedance spectra (EIS) were detected on an electrochemical system (Solartron 1255 B frequency response analyzer and Solartron SI 1287 electrochemical interface) with 0.1 mol L<sup>-1</sup> KCl solution as the electrolyte, FTO/ZnO/CPAN(1:1) or FTO/ZnO electrode as the working electrode, Pt as the counter electrode, and saturated calomel electrode (SCE) as the reference electrode, respectively. The ZnO/CPAN(1:1) and ZnO films were coated on the FTO substrates (fluorine-doped SnO<sub>2</sub>, 15 Ω/sq) using a doctor-blade method. The photocurrent analysis was carried out on a CHI 660E electrochemical system without bias under visible light irradiation. A three electrode quartz cell was used for measurement with Pt as the counter electrode, Ag/AgCl as reference electrode, the thin film of ZnO/CPAN(1:1) or pure ZnO on indium-tin oxide (ITO) glass as the working electrode, and 0.2 mol L<sup>-1</sup> Na<sub>2</sub>SO<sub>4</sub> aqueous solution as the electrolyte, respectively. The BET surface area was measured by a Micromeritics TriStar II 3020 surface area and porosity system using nitrogen as adsorption gas at 77 K. The electron spin resonance spectra (ESR) of the photocatalyst samples were carried out on a Bruker model ESR JES-FA200 spectrometer with a microwave frequency of 9.07 GHz and modulation frequency of 100.00 kHz.

#### 2.4. Photocatalytic activity test

The photodegradation of MO or sodium phenolate was used to evaluate the visible-light photocatalytic activity of the ZnO/CPAN nanocomposites and other photocatalysts under a 300 W iodine tungsten lamp (Philips Co.) with a 400 nm cut-off filter to ensure the visible light irradiation, and the light intensity on the surface of the suspension was ca. 85.0 mW cm<sup>-2</sup> measured by an optical power meter (Model 842-PE, Newport Corporation, USA). 0.12 g or 0.06 g of the photocatalyst was added into 120 mL of aqueous MO solution (20 mg L<sup>-1</sup>) or sodium phenolate solution (50 mg L<sup>-1</sup>) in a cylindrical glass reactor. The aqueous suspension was continuously stirred for 120 min in dark in order to establish an adsorption-desorption equilibrium. Then, the suspension was exposed to visible light radiation. The glass reactor was open to ensure the enough oxygen into the system. During irradiation, the samples were taken out at given time intervals and separated by high speed centrifugation. The upper clear solutions were analyzed using a TU-1901 UV-vis spectrophotometer (Beijing Purkinje General Instrument Co., Ltd., China) to record the absorbency variations at the maximum absorption band of 464 nm for MO or 234 nm for sodium phenolate at natural pH conditions. The symbols of  $c_0$  and  $c$  represent the concentrations of MO solutions before and after irradiation, respectively. For comparison, the photodegradation of MO in the dark in the presence of the photocatalyst and under visible light irradiation without the photocatalyst were also carried out.

To assess the photocatalytic stability of ZnO/CPAN nanocomposites, they were reused for the above photodegradation experiment. After every cycle, the ZnO/CPAN nanocomposites were filtered,

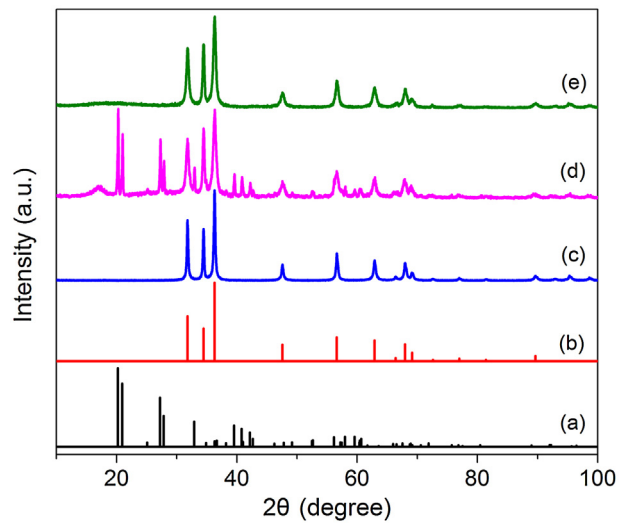


**Fig. 1.** XRD patterns of Zn(OH)<sub>2</sub> (PDF# 01-089-0138) (a), ZnO (PDF# 01-089-0510) (b), pure ZnO (c), the precursor of ZnO/PAN(1:1) (d) and ZnO/CPAN(1:1) (e).

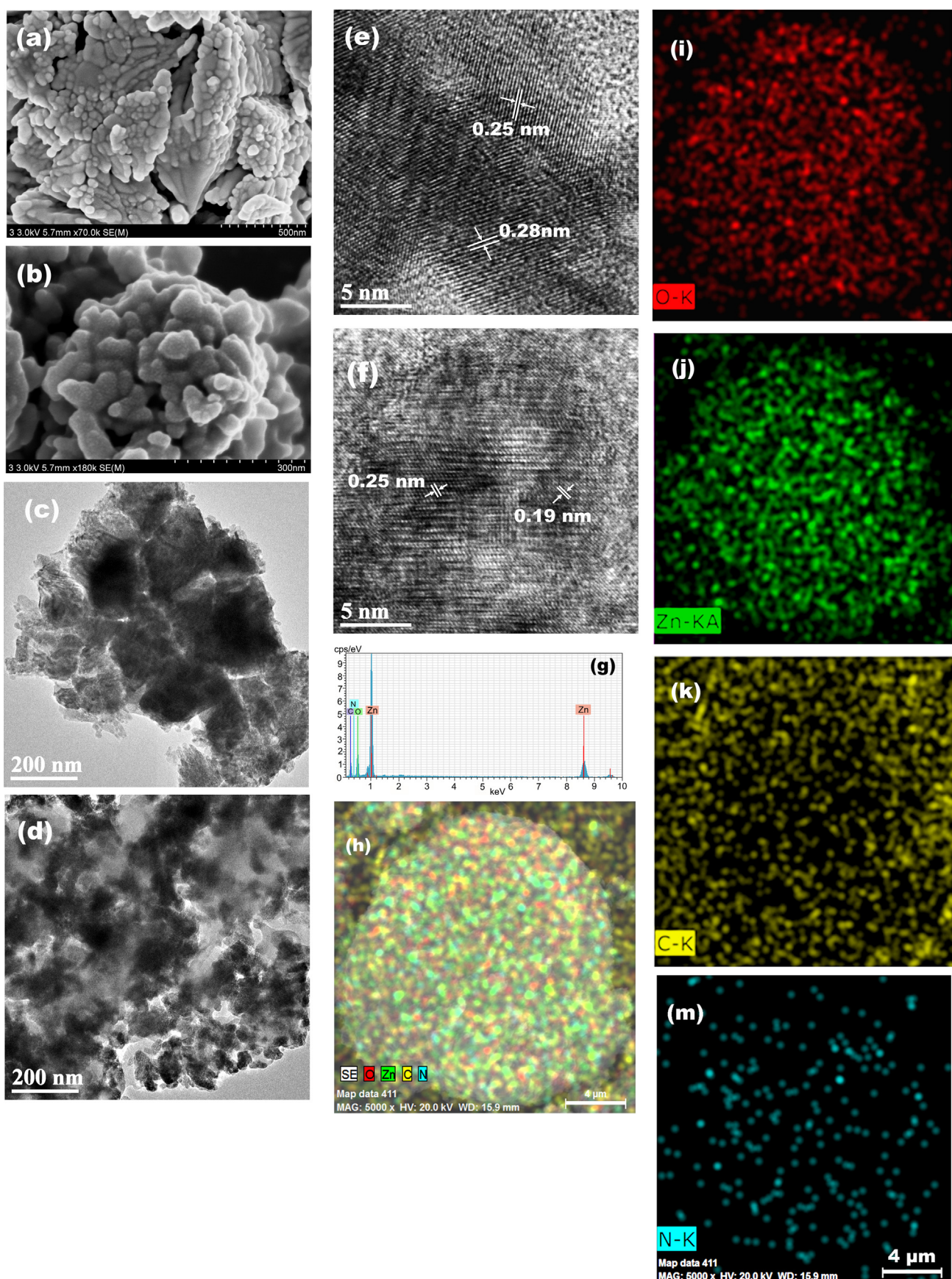
washed by a large amount of water, then was dried at 60 °C for 3 h and reused in the next cycle.

## 3. Results and discussion

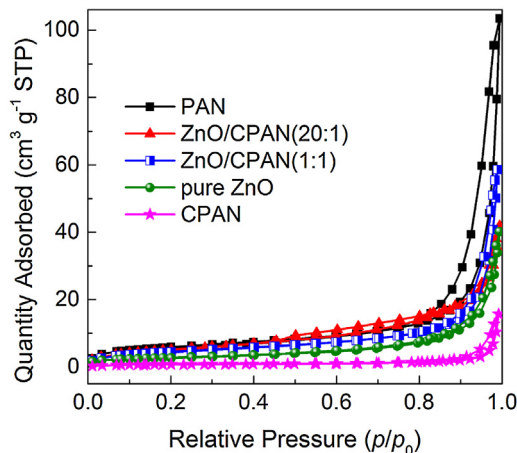
### 3.1. Structure and morphology of ZnO/CPAN nanocomposites

Fig. 1 illustrates the XRD patterns of the precursor of ZnO/PAN(1:1), ZnO/CPAN(1:1) and pure ZnO. For the precursor of ZnO/PAN(1:1), the diffraction peak at ~17° is associated with the (100) plane of PAN [35], the diffraction peaks at 20.18°, 20.91°, 25.07°, 27.22°, 27.80°, 32.89°, 39.54°, 40.80°, 42.16°, 52.65°, 57.97°, 59.55° and 60.66° are ascribed to (011), (101), (110), (111), (102), (112), (120), (113), (211), (221), (131), (124) and (302) planes of Zn(OH)<sub>2</sub> (PDF# 01-089-0138), the diffraction peaks at 31.78°, 34.43°, 36.26°, 47.55°, 56.61°, 62.88°, 66.40°, 67.97°, 69.11°, 72.59°, 76.98°, and 89.64° are attributed to (100), (002), (101), (102), (110), (103), (200), (112), (201), (004), (202) and (203) planes of ZnO with the hexagonal wurtzite phase (PDF# 01-089-0510), respectively. This result reveals the co-existence of PAN, Zn(OH)<sub>2</sub> and ZnO in the precursor of ZnO/PAN. For ZnO/CPAN(1:1), the characteristic peaks of Zn(OH)<sub>2</sub> disappear and the characteristic peaks of pure ZnO can be observed in the XRD pattern, while the diffraction peak of PAN significantly decreases, indicating that Zn(OH)<sub>2</sub> was completely decomposed into ZnO and the cyclization of PAN occurred to form CPAN. Compared with pure ZnO, ZnO/CPAN(1:1) displays the same XRD spectrum, confirming that the cyclization reaction of PAN does not affect the crystal structure of ZnO. According to Scherrer's formula, the mean sizes of the ZnO/CPAN(1:1) and pure ZnO are 17.3 nm and 39.8 nm, respectively, indicating that the presence of CPAN can significantly inhibit the growth of ZnO nanocrystals, leading to decreasing the mean size of ZnO/CPAN nanocomposites.

The morphologies of pure ZnO and ZnO/CPAN(1:1) were observed by SEM and TEM as shown in Fig. 2. It can be clearly seen



**Fig. 2.** SEM images of pure ZnO (a) and ZnO/CPAN(1:1) (b), TEM images of pure ZnO (c) and ZnO/CPAN(1:1) (d), HRTEM images of pure ZnO (e) and ZnO/CPAN(1:1) (f), EDX of ZnO/CPAN(1:1) (g), element mapping images of ZnO/CPAN(1:1) (h) and corresponding element mapping images of O, Zn, C and N (i-m).



**Fig. 3.** N<sub>2</sub> adsorption–desorption isotherms of pure ZnO, ZnO/CPAN(20:1), ZnO/CPAN(1:1), PAN, and CPAN.

that pure ZnO particles are highly aggregated (Fig. 2a and c). The ZnO/CPAN (1:1) particles (Fig. 2b and d) show well dispersed and their mean size is obviously smaller than that of pure ZnO particles, which is consistent with the XRD result. As shown in Fig. 2e and f, the grain boundaries of ZnO/CPAN (1:1) are not as clear as those of pure ZnO particles due to the presence of CPAN. The lattice spacing of 0.28 nm, 0.25 nm and 0.19 nm agrees well with the (100), (101) and (102) crystallographic plane in the hexagonal ZnO crystal, respectively. It can be seen from the EDX image (Fig. 2g) that the ZnO/CPAN(1:1) nanocomposite is composed of O, Zn, C and N elements, which are ascribed to ZnO and CPAN, respectively. The corresponding element mapping images of O, Zn, C and N are shown in Fig. 2h–m. All of these elements are overlaid mutually and exhibit homogeneous distribution, indicating that ZnO and CPAN are well-dispersed in the investigated sample.

The nitrogen adsorption–desorption isotherms of pure ZnO, ZnO/CPAN(20:1), ZnO/CPAN(1:1), PAN, and CPAN are presented in Fig. 3. The BET specific surface areas of pure ZnO, ZnO/CPAN(20:1), ZnO/CPAN(1:1), PAN, and CPAN were found to be 9.9, 19.3, 16.5, 20.9, and 2.6 m<sup>2</sup> g<sup>-1</sup>, respectively. The result reveals that the heat-treatment makes the specific surface area of PAN decrease sharply from 20.9 to 2.6 m<sup>2</sup> g<sup>-1</sup> due to the softening and shrinkage of PAN. However, the specific surface area of ZnO/CPAN nanocomposites are obviously larger than that of pure ZnO and CPAN because the presence of PAN suppress the growth of ZnO crystals, meanwhile, ZnO reduces the shrinkage of PAN in the calcination process.

### 3.2. FTIR analysis of ZnO/CPAN nanocomposites

The FT-IR spectra of PAN, CPAN, pure ZnO and ZnO/CPAN nanocomposites heat-treated at different temperatures in nitrogen atmosphere are shown in Fig. 4. In the spectrum of PAN (Fig. 4a), the peaks at 2940, 1450 and 1357 cm<sup>-1</sup> are ascribed to methylene/methine C–H stretching vibration, methylene C–H bend vibration and methine C–H bend vibration, the peak at 1250 cm<sup>-1</sup> is attributed to skeletal C–C vibrations in PAN molecules [36]. The peak at 2244 cm<sup>-1</sup> belongs to C≡N stretching vibration. The wide and strong band at 448 cm<sup>-1</sup> is assigned to Zn–O stretching mode of ZnO (Fig. 4c). Compared with the FT-IR spectrum of PAN, some obvious changes can be observed in the FT-IR spectrum of CPAN (Fig. 4b). The characteristic peak of C≡N at 2244 cm<sup>-1</sup> decreases significantly, while new intense peaks at 1580 and 1386 cm<sup>-1</sup> attributed to C=N and C–N stretching vibration appear, which indicates the cyclization reaction between adjacent C≡N groups occurs [37]. Simultaneously, the peak of methylene at 1450 cm<sup>-1</sup> obvi-

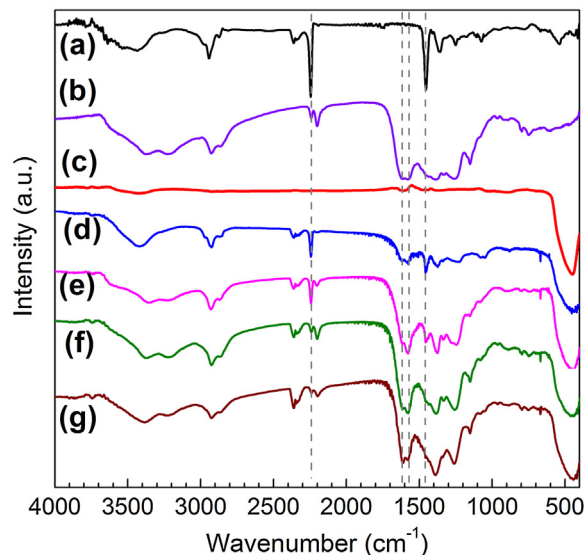


**Fig. 4.** FT-IR spectra of PAN (a), CPAN (b), pure ZnO (c) and ZnO/CPAN (1:1) nanocomposites heat-treated at temperature of 210 °C (d), 230 °C (e), 250 °C (f) and 270 °C (g) for 1 h in nitrogen atmosphere.

ously decreases, accompanied with the appearance of a new intense peak at 1610 cm<sup>-1</sup> attributed to C=C stretching vibration, revealing the occurrence of dehydrogenation reaction when PAN was heated in nitrogen environment. In addition, the peak at 2200 cm<sup>-1</sup> is attributed to the conjugation of C≡N with C=C group [38,39]. In the spectra of ZnO/CPAN nanocomposites (Fig. 4d–g), all the characteristic peaks of CPAN and ZnO can be easily observed, revealing that the as-prepared ZnO/CPAN nanocomposites are composed of CPAN and ZnO. With the increase of the heat-treatment temperature, the intensity of band of C≡N at 2240 cm<sup>-1</sup> reduces while the intensity of bands of C≡N and C=C group at 1580 and 1610 cm<sup>-1</sup> increase, revealing that the amount of C≡N groups decreases, and the amount of C≡N and C=C groups increases.

### 3.3. Surface state analysis of ZnO/CPAN nanocomposites

XPS analyses were conducted to probe the surface chemical composition and the elemental chemical states of the as-prepared samples. Fig. 5a displays the comparison of the survey spectra of ZnO/CPAN (1:1), pure ZnO and CPAN. The elements of C, O, Zn and N can be detected on the surface of ZnO/CPAN (1:1). The C element results from CPAN molecules and the adventitious element carbon. The elements of Zn and O are assigned to ZnO. The N element is attributable to CPAN molecules. Fig. 5b–e presents the high-resolution XPS spectra of C 1s, N 1s, O 1s and Zn 2p of ZnO/CPAN (1:1), respectively. The C 1s spectra of CPAN and ZnO/CPAN (Fig. 5b) can be deconvoluted into four components at about 284.6, 285.7, 286.3, and 288.2 eV, respectively. The peak located at 284.6 eV is assigned to C–C bonds of CPAN or adventitious elemental carbon [40,41]. The peak at 285.7 eV is corresponded to sp<sup>2</sup>-hybridized carbon atoms bonded to N (N–C≡N) [42]. The peak at 286.3 eV is attributed to C–C=C bonds of CPAN, and the peak at 288.2 eV is assigned to C–O and C=O. As shown in Fig. 5c, the N 1s XPS spectrum of CPAN can be fitted into one main peak at 398.4 eV which is attributed to the sp<sup>2</sup>-hybridized nitrogen atom bonded to two carbon atoms (C≡N=C) [25], while the binding energy value of N 1s in ZnO/CPAN was observed at 399.0 eV, shifting towards the higher energy region by 0.6 eV. The similar result can be seen in the Zn 2p spectra of the pure ZnO and ZnO/CPAN (Fig. 5e). The Zn 2p spectrum of the pure ZnO displays doublet peaks at 1021.4 and 1044.7 eV, which are assigned to Zn 2p<sub>3/2</sub> and 2p<sub>1/2</sub> of Zn<sup>2+</sup> in

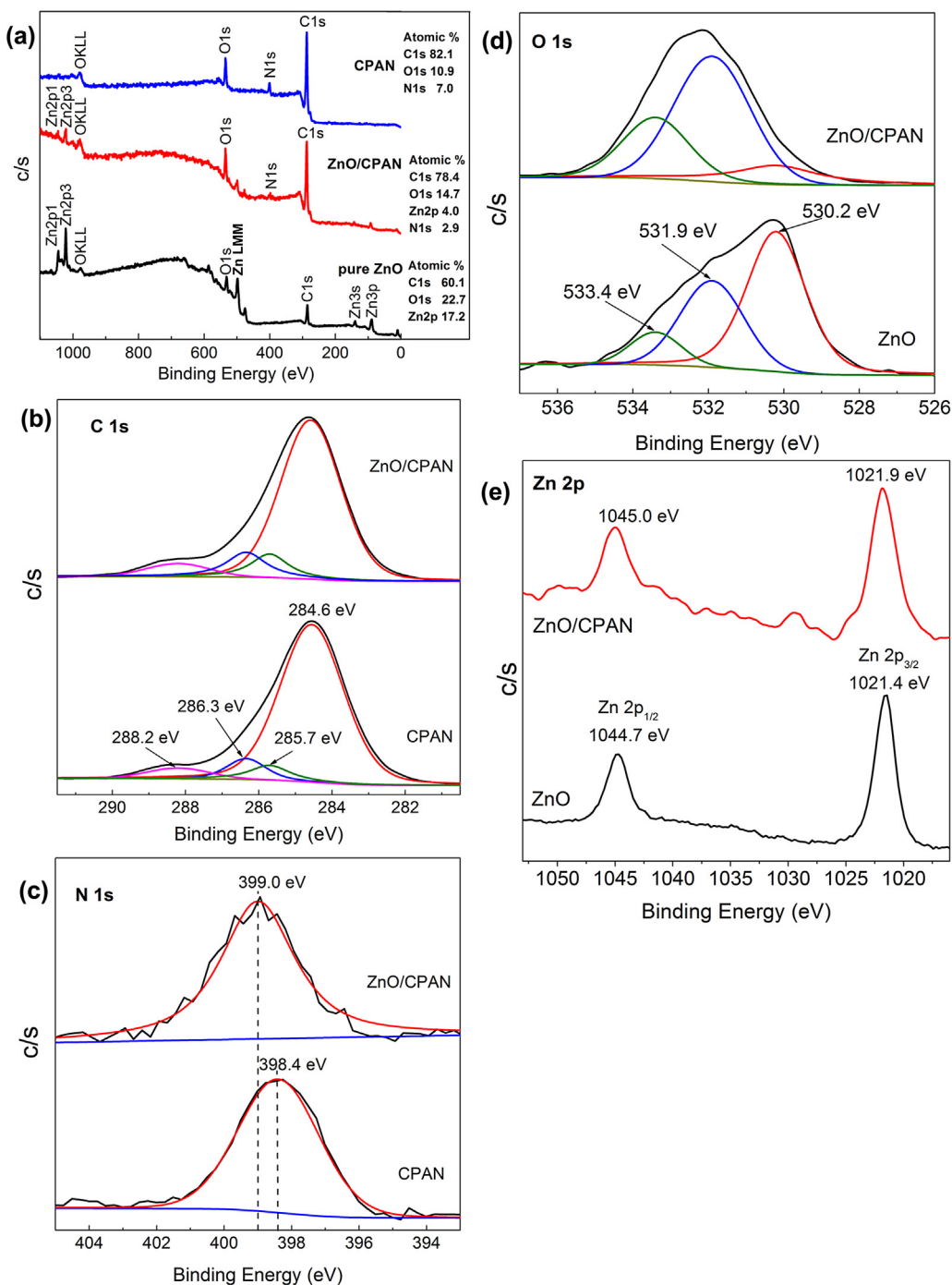


**Fig. 5.** XPS survey spectra (a) and high-resolution XPS spectra of C 1s (b), N 1s (c), O 1s (d) and Zn 2p (e) of ZnO/CPAN (1:1), CPAN and ZnO.

ZnO. The corresponding peaks of Zn 2p in ZnO/CPAN are observed at 1021.9 and 1045.0 eV. Such a shift towards the higher energy region for N 1s and Zn 2p in ZnO/CPAN may be attributed to the interaction between nitrogen atom and Zn<sup>2+</sup> ion. In the O 1s XPS spectra of Fig. 5d, the peak located at 530.2 eV is assigned to O<sup>2-</sup> ions in the Zn-O bonds of the wurtzite ZnO structure [43]. The peak located at 533.4 eV is related to the chemisorbed oxygen or OH group absorbed onto the surface of the photocatalyst [44,45]. The peak at 531.9 eV is attributed to O<sup>2-</sup> in the oxygen-deficient regions within the ZnO matrix [46], and the intensity of this peak is correlated with the variation in the concentrations of oxygen defects (vacancies) [12]. It can be clearly seen that the intensity of the peak at 530.2 eV for ZnO/CPAN is much weaker than that of

pure ZnO, while the intensity of the peak at 531.9 for ZnO/CPAN is much stronger than that of pure ZnO, revealing that the quantity of oxygen defects in ZnO/CPAN is more than that of pure ZnO. This may result from the calcination of ZnO/CPAN in nitrogen environment. Because the dehydrogenation reaction of PAN can easily occur in nitrogen atmosphere to produce hydrogen, and hydrogen probably seizes the oxygen atom on the surface of ZnO during the calcination process, leading to the formation of oxygen defects in ZnO/CPAN. Additionally, compared with pure ZnO, the amount of oxygen or OH group absorbed onto the surface of ZnO/CPAN significantly increases. The presence of the oxygen vacancies and the oxygen or OH group absorbed onto the surface of ZnO/CPAN are helpful to enhance its photocatalytic activity [12,45].

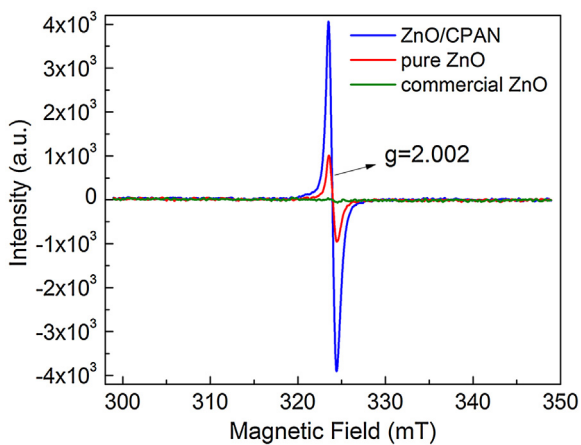


**Fig. 6.** ESR spectra of commercial ZnO, pure ZnO, ZnO/CPAN(1:1).

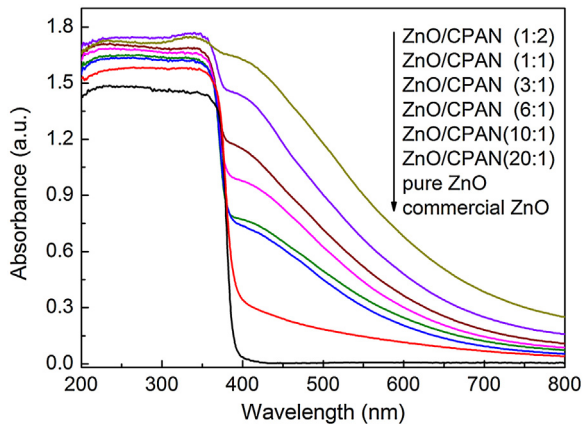


**Fig. 7.** UV-vis diffuse reflectance spectra of pure ZnO and ZnO/CPAN nanocomposites with different mass ratios of ZnO to PAN.

To further detect the defects of oxygen vacancy of photocatalyst, ESR spectra were recorded and presented in Fig. 6. The commercial ZnO does not show any apparent signal, indicating it does not contain unpaired electrons. However, the pure ZnO prepared in nitrogen atmosphere displays a clear signal centered at  $g=2.002$ , which is assigned to single electron trapped oxygen vacancy [47–49]. For comparison, a symmetrical, sharp signal in the spectrum of ZnO/CPAN gives clear evidence that the as-obtained ZnO/CPAN contains high concentration of oxygen vacancies, which is accordant with the results of XPS spectra.

### 3.4. UV-vis DRS and PL spectra of ZnO/CPAN nanocomposites

Fig. 7 displays the UV-vis diffuse reflectance spectra of pure ZnO and ZnO/CPAN nanocomposites with different mass ratios of ZnO to PAN. As shown in Fig. 7, commercial ZnO is a typical UV-light-driven photocatalyst and shows almost no absorption in the visible light region, while the pure ZnO prepared in nitrogen atmosphere exhibits obvious light absorption in the visible range due to the presence of the surface oxygen vacancies. Compared with the above-mentioned ZnO samples, ZnO/CPAN nanocomposites show significantly enhanced light absorption in the whole light region, especially in the visible light range. Furthermore, the absorbance of the ZnO/CPAN nanocomposites increases with the CPAN amount increasing. The results indicate that CPAN can easily absorb visible light, which is advantageous to improve the visible-light photocatalytic activity of as-prepared nanocomposites.

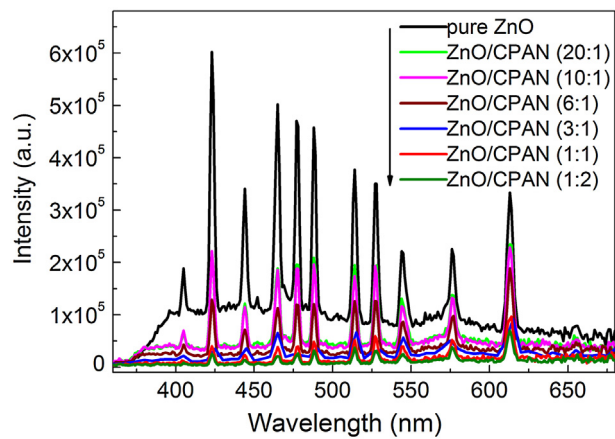


**Fig. 8.** PL emission spectra of pure ZnO and ZnO/CPAN nanocomposites with different mass ratios of ZnO to PAN.

PL spectra of pure ZnO and ZnO/CPAN nanocomposites with different mass ratios of ZnO to PAN are presented in Fig. 8. Pure ZnO shows significantly high PL intensity due to its high recombination probability of the photo-generated electrons and holes, while the ZnO/CPAN nanocomposites have much lower PL intensity than that of pure ZnO. In addition, the PL intensity of the as-prepared ZnO/CPAN nanocomposites decreases with the increment of the amount of CPAN. The remarkable reduction of PL intensity reveals that the recombination probability of photo-generated electron/hole pairs in ZnO/CPAN greatly decreases and their separation efficiency obviously increases, which is attributed to the high electron mobility of spatially extended  $\pi$ -bonding conjugated system of CPAN. The more amount of conjugated CPAN, the easier transfer of photo-generated electron/hole pairs between CPAN and ZnO accordingly, and the more favorable to the photocatalytic reaction.

### 3.5. Photoelectrochemical analysis of ZnO/CPAN nanocomposites

The photo-electrochemical property is widely used to investigate the charge transfer and separation of photo-generated electron–hole pairs at semiconductor/electrolyte interface [50]. As shown in Fig. 9(a), the arc radius on the EIS Nyquist plots of ZnO/CPAN(1:1) is obviously smaller than that of pure ZnO, revealing that both the electron-hole pair separation efficiency and the interface charge transfer efficiency are significantly improved in ZnO/CPAN(1:1). Moreover, the photocurrent transient responses for commercial ZnO, pure ZnO and ZnO/CPAN(1:1) electrodes for several switch-on and switch-off cycles under intermittent visible light irradiation were measured and shown in Fig. 9(b). It can be seen that no significant photocurrent was observed in the dark for both electrodes, while the photocurrent densities increase sharply upon light illumination. Noticeably, ZnO/CPAN(1:1) displays much higher photocurrent density than that of pure ZnO and commercial ZnO. The photocurrent enhancement indicates a more effective separation of photo-generated electrons/holes pairs and consequently high photocatalytic activity [51], which could be attributed to the interaction of ZnO and CPAN.

### 3.6. Visible-light photocatalytic activity of ZnO/CPAN nanocomposites

The photocatalytic activities of the as-prepared photocatalysts were evaluated via MO or sodium phenolate photodegradation experiments under visible light irradiation and the results are shown in Fig. 10. As shown in Fig. 10(a), in the adsorption process,

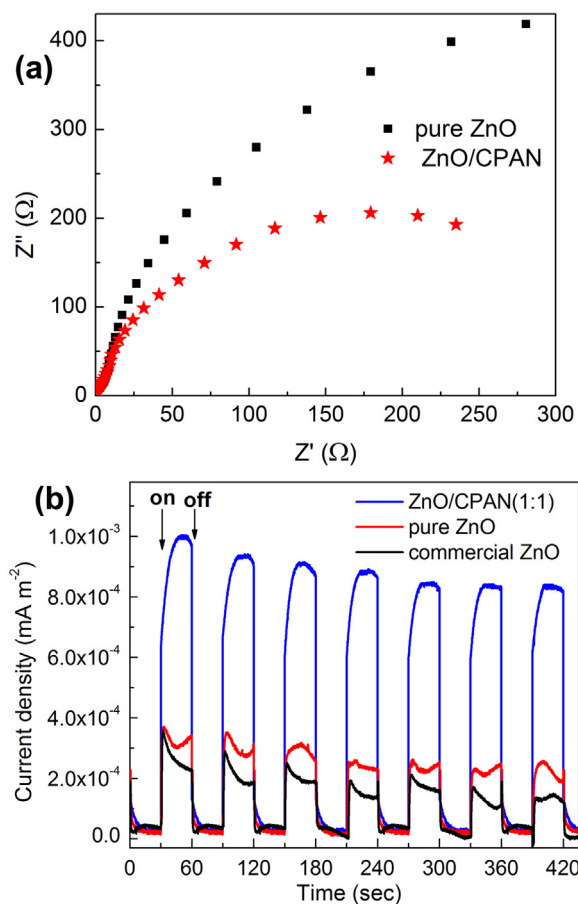


**Fig. 9.** EIS of FTO/ZnO and FTO/ZnO/CPAN electrodes with an applied bias potential of 0.5 V (a) and transient photocurrent response of commercial ZnO, pure ZnO and ZnO/CPAN(1:1) under visible light irradiation (b).

there is a little concentration reduction of MO in the presence of pure ZnO, while obvious concentration reduction of MO can be observed in the presence of ZnO/CPAN nanocomposites or CPAN, revealing that MO is easily adsorbed on the surface of ZnO/CPAN nanocomposites and CPAN. The high adsorption amount will be favorable to the photodegradation of MO [52,53]. It can be seen that the degradation of MO under visible light irradiation without photocatalyst or in the dark in the presence of ZnO/CPAN(1:1) nanocomposites are negligible. After visible light irradiation for 60 min, only 5.3% of MO was degraded in the presence of pure ZnO, while MO was obviously degraded in the presence of the ZnO/CPAN nanocomposites, e.g., 95% of MO was degraded by ZnO/CPAN (1:1), indicating that the ZnO/CPAN nanocomposites exhibit efficient visible-light photocatalytic activity. With the increment of the amount of CPAN in the ZnO/CPAN nanocomposites or heat-treatment temperature (Fig. 10b), the visible light photocatalytic activity of the ZnO/CPAN nanocomposites initially increases and then decreases, and the optimum ZnO/CPAN mass ratio in the nanocomposites and heat-treatment temperature are 1:1 and 250 °C, respectively. Fig. 10(c) reveals that colorless sodium phenolate can be also efficiently photodegraded by ZnO/CPAN (1:1), similar to the MO photodegradation.

Fig. 11 displays the comparison of the MO photodegradation in the presence of ZnO/CPAN (1:1) heated at 250 °C and the typical visible-light photocatalysts such as AgBr, Ag<sub>3</sub>PO<sub>4</sub> and g-C<sub>3</sub>N<sub>4</sub>. The MO photodegradation rate in the presence of ZnO/CPAN (1:1) is much larger than those in the presence of AgBr, Ag<sub>3</sub>PO<sub>4</sub> and g-C<sub>3</sub>N<sub>4</sub>, and the apparent rate constant for MO photodegradation in the presence of ZnO/CPAN (1:1) ( $0.361 \text{ h}^{-1}$ ) is 1.28, 5.84 and

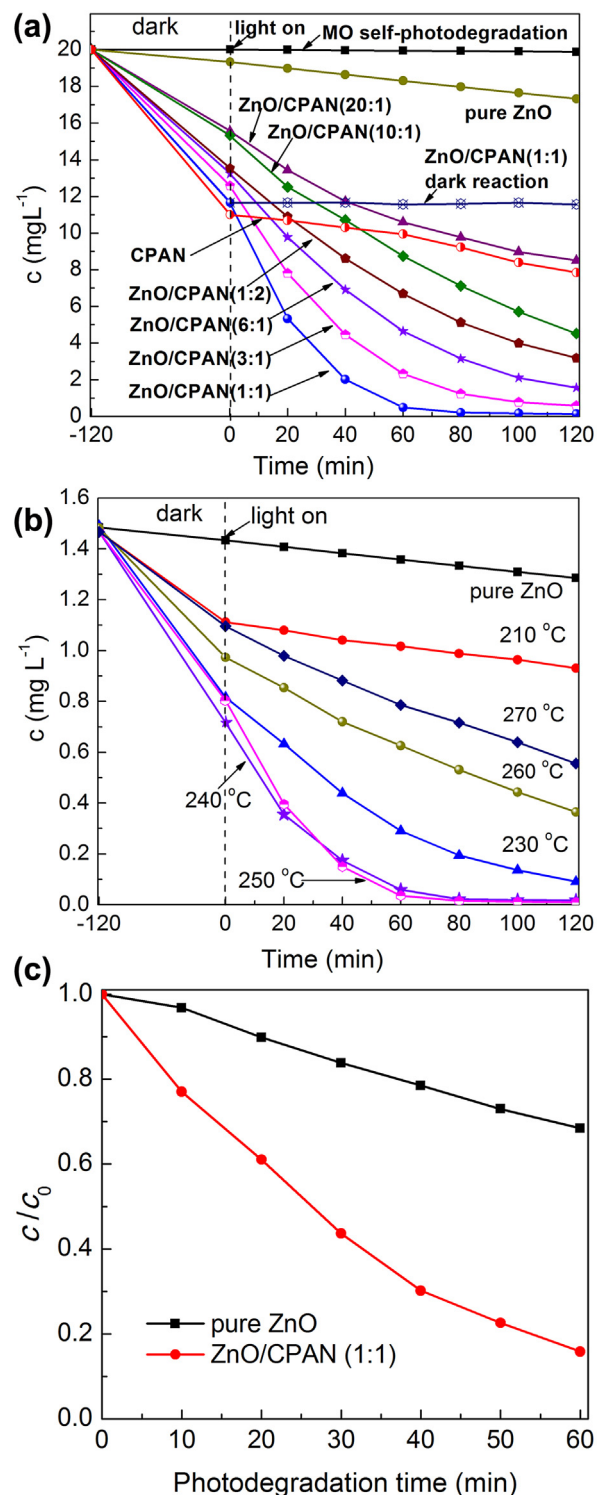


**Fig. 10.** MO adsorption in dark and photodegradation in the presence of pure ZnO and ZnO/CPAN nanocomposites prepared 250 °C with different mass ratios of ZnO to PAN (a) or in the presence of ZnO/CPAN (1:1) prepared at different temperatures (b) under visible light irradiation (MO concentration: 20 mg L<sup>-1</sup>, photocatalyst concentration: 1.0 g L<sup>-1</sup>), and sodium phenolate photodegradation in the presence of pure ZnO and ZnO/CPAN (1:1) under visible light of different wavelength (sodium phenolate concentration: 50 mg L<sup>-1</sup>, photocatalyst concentration: 0.5 g L<sup>-1</sup>) (c).

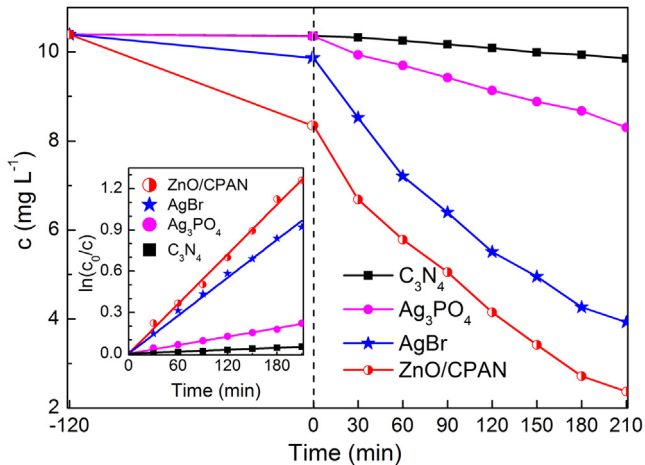


**Fig. 11.** Comparison of MO photodegradation in the presence of  $\text{ZnO/CPAN}$  (1:1),  $\text{AgBr}$ ,  $\text{Ag}_3\text{PO}_4$  and  $\text{g-C}_3\text{N}_4$  (MO concentration:  $10 \text{ mg L}^{-1}$ , photocatalyst concentration:  $0.2 \text{ g L}^{-1}$ ).

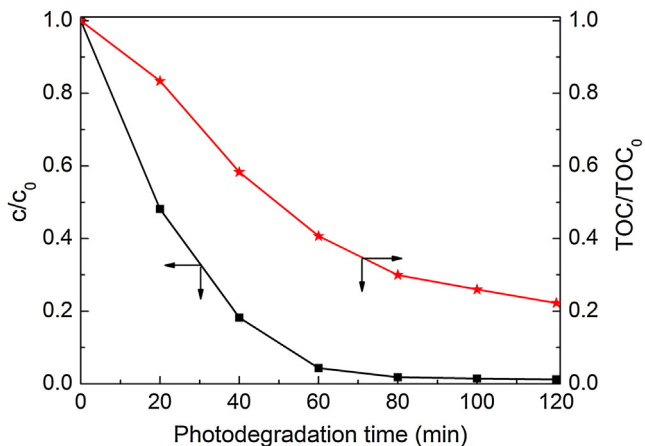


**Fig. 12.** Photodegradation and TOC removal of MO solution ( $20 \text{ mg L}^{-1}$ , 120 mL) in the presence of  $\text{ZnO/CPAN}$  (1:1) ( $1 \text{ g L}^{-1}$ ) under visible-light irradiation.

25.8 times of the corresponding value in the presence of  $\text{AgBr}$  ( $0.282 \text{ h}^{-1}$ ),  $\text{Ag}_3\text{PO}_4$  ( $0.0618 \text{ h}^{-1}$ ) or  $\text{g-C}_3\text{N}_4$  ( $0.0140 \text{ h}^{-1}$ ), meaning that  $\text{ZnO/CPAN}$  (1:1) exhibits much higher visible-light photocatalytic activity than these typical visible-light photocatalysts.

In order to further investigate the mineralization efficiency of MO catalyzed by  $\text{ZnO/CPAN}$  (1:1), total organic carbon (TOC) of the aqueous solution of MO in the photodegradation process was measured, and the result is shown in Fig. 12. Similar to the MO photodegradation rate, TOC value of MO degradation solution decreases gradually with the increase of photodegradation time, indicating that MO can be not only decolorized but also mineralized efficiently in the presence of  $\text{ZnO/CPAN}$  nanocomposites.

As another important performance for the practical application of a photocatalyst, the photocatalytic stability of  $\text{ZnO/CPAN}$  (1:1) was evaluated by the recycling experiments of MO photodegradation, and the results are shown in Fig. 13. It can be seen that the MO can be totally photodegraded in each cycle, revealing that  $\text{ZnO/CPAN}$  nanocomposites exhibit excellent visible-light photocatalytic activity and stability.

Furthermore, the effects of ethylene diamine tetraacetic acid (EDTA, holes scavenger) and dimethyl sulfoxide (DMSO, electrons scavenger) on MO photodegradation were investigated for determining the main oxidative species in the photocatalytic process, and the results are displayed in Fig. 14. It can be seen that the

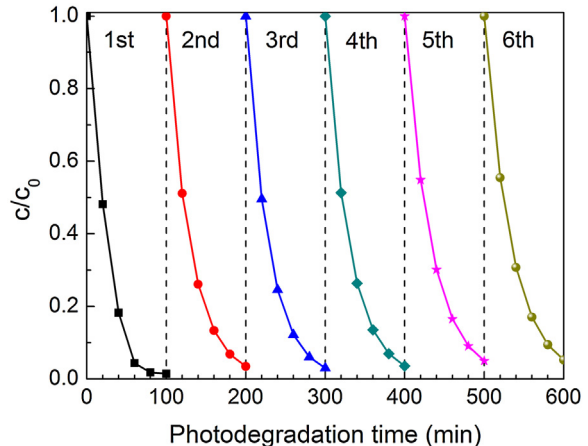


**Fig. 13.** Cycling runs of  $\text{ZnO/CPAN}$  (1:1) for MO photodegradation under visible-light irradiation (MO concentration:  $20 \text{ mg L}^{-1}$ , photocatalyst concentration:  $1 \text{ g L}^{-1}$ ).

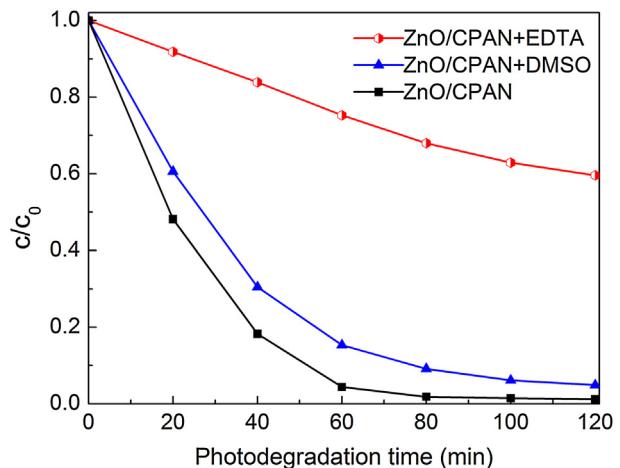


**Fig. 14.** Effects of EDTA and DMSO on the photodegradation rate of MO photocatalyzed by  $\text{ZnO/CPAN}$  (1:1) under visible-light irradiation (MO concentration:  $20 \text{ mg L}^{-1}$ , photocatalyst concentration:  $1 \text{ g L}^{-1}$ ).

MO photodegradation is greatly suppressed by EDTA but slightly decreased by DMSO, revealing that the photogenerated holes are the main active species for MO photodegradation catalyzed by  $\text{ZnO/CPAN}$  nanocomposites.

### 3.7. Visible-light photocatalytic mechanism of $\text{ZnO/CPAN}$ nanocomposites

The band gap energies of photocatalysts can be obtained from the plot of  $(\alpha h\nu)^2$  versus the photon energy ( $h\nu$ ) based on the equation  $(\alpha h\nu)^2 = A(h\nu - E_g)$  [54]. Fig. 15(a) shows that the band gap energies of commercial  $\text{ZnO}$ , pure  $\text{ZnO}$ ,  $\text{ZnO}$  in  $\text{ZnO/CPAN}$  (1:1) and CPAN are 3.24, 3.17, 2.93 and 2.26, respectively. The narrower band gap of  $\text{ZnO}$  (2.93 eV) in  $\text{ZnO/CPAN}$  (1:1) can be attributed to the more quantity of oxygen defects since the oxygen atom on the surface of  $\text{ZnO/CPAN}$  nanocomposites can be easily despoiled by hydrogen from the dehydrogenation reaction of PAN in nitrogen atmosphere, meaning that it can absorb visible light and be activated to generate electrons and holes for the MO photodegradation.

The valence band X-ray photoelectron spectroscopy (VB-XPS) is a useful tool to investigate the band structure of semiconductors. The VB-XPS spectra of  $\text{ZnO}$  in  $\text{ZnO/CPAN}$  (1:1) and CPAN are shown in Fig. 15(b) and (c), respectively. The potentials of the valence band (VB) of  $\text{ZnO}$  in  $\text{ZnO/CPAN}$  (1:1) and highest occu-

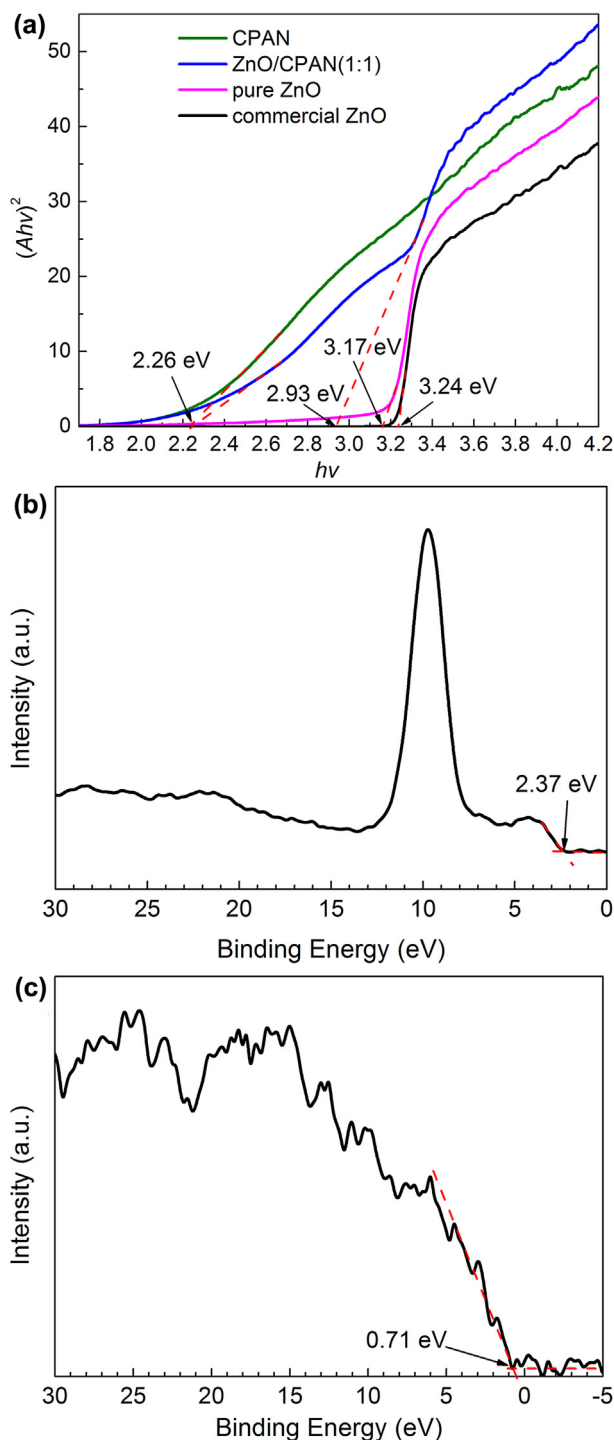
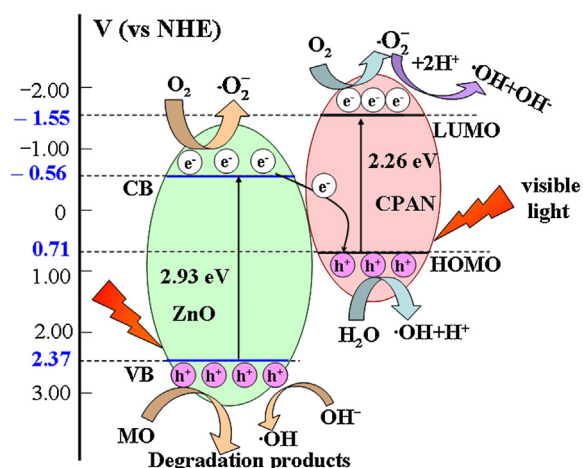


**Fig. 15.** The plots of  $(\alpha h\nu)^2$  versus the photon energy ( $h\nu$ ) for the as-prepared samples (a) and the VB-XPS spectra of ZnO (b) and CPAN (c).

occupied molecular orbital (HOMO) of CPAN are about 2.37 and 0.71 V, respectively. According to the equation  $E_{CB} = E_{VB} - E_g$ , the position of the conduction band (CB) edge of ZnO in ZnO/CPAN(1:1) and lowest unoccupied molecular orbital (LUMO) of CPAN can be obtained at about  $-0.56$  and  $-1.55$  V, respectively [55].

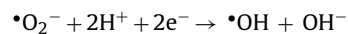
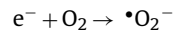
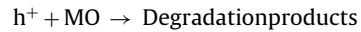
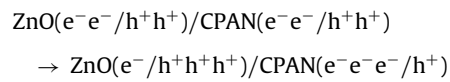
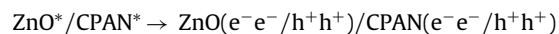
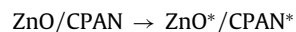
Under visible light irradiation, both ZnO and CPAN in ZnO/CPAN nanocomposites can be activated to produce photo-generated holes and electrons. Generally, the photo-generated electrons in LUMO of CPAN ( $-1.55$  V) can be easily injected to conduction band of ZnO ( $-0.56$  V), and the photo-generated holes in valence band of



**Scheme 3.** Schematic description of visible-light photocatalytic mechanism of ZnO/CPAN nanocomposites.

ZnO (2.37 V) can easily transfer to HOMO of CPAN (0.71 V). Due to the weak oxidation ability of the photo-generated holes in HOMO of CPAN (0.71 V), they are not able to act as the main active species for MO photodegradation. However, the carriers trapping experiments reveal the photo-generated holes not electrons as the main active species for MO photodegradation, indicating that the transfer of photogenerated holes and electrons does not follow the above-described mechanism and probably follows the Z-scheme mechanism widely reported in literature [56–58], i.e., the photo-generated electrons in conduction band of ZnO transfer to HOMO of CPAN, leading the more photo-generated holes and electrons to aggregating in valence band of ZnO (2.37 V) and LUMO of CPAN ( $-1.55$  V) respectively. The photo-generated holes in valence band of ZnO (2.37 V) possess enough oxidizing ability to directly degrade MO, and the electrons in LUMO of CPAN can react with O<sub>2</sub> to form O<sub>2</sub><sup>-</sup> for degrading MO.

On the basis of the above discussion, the possible photocatalytic mechanism of the ZnO/CPAN nanocomposites under visible light irradiation can be schematically presented in Scheme 3, and the probable reaction for the MO photodegradation can be displayed as follows.



#### 4. Conclusion

A facile method has been developed for preparing well-dispersed ZnO/CPAN nanocomposite as an efficient visible-light

photocatalyst. The CPAN molecules in the ZnO/CPAN nanocomposite significantly decrease the mean size of ZnO nanocrystals, increase the quantity of oxygen defects in ZnO particles, improve the absorbance of ZnO in the whole wavelength range especially in the visible-light range, and obviously reduce the recombination probability of photo-generated electron/hole pairs. The ZnO/CPAN nanocomposite exhibits excellent visible-light photocatalytic stability and much higher visible-light photocatalytic activity than the typical visible-light photocatalysts such as AgBr, Ag<sub>3</sub>PO<sub>4</sub> and g-C<sub>3</sub>N<sub>4</sub>. Due to its low preparation cost and excellent photocatalytic performances, the ZnO/CPAN nanocomposite may be an important visible-light photocatalyst for practical application in a large scale.

## Acknowledgements

This work was supported by The National Natural Science Foundation of China (No. 21271061) and Natural Science Foundation of Hebei Province (Nos. B2014208103 and 15961401D).

## References

- [1] X. Li, J. Yu, M. Jaroniec, Hierarchical photocatalysts, *Chem. Soc. Rev.* 45 (2016) 2603–2636.
- [2] M.R. Hoffmann, S.T. Martin, W. Choi, D.W. Bahnemann, Environmental applications of semiconductor photocatalysis, *Chem. Rev.* 95 (1995) 69–96.
- [3] S. Livraghi, M.C. Paganini, E. Giamello, A. Selloni, C.D. Valentini, G. Pacchioni, Origin of photoactivity of nitrogen-doped titanium dioxide under visible light, *J. Am. Chem. Soc.* 128 (2006) 15666–15671.
- [4] Y. Li, W. Cui, L. Liu, R. Zong, W. Yao, Y. Liang, Y. Zhu, Removal of Cr(VI) by 3D TiO<sub>2</sub>-graphene hydrogel via adsorption enriched with photocatalytic reduction, *Appl. Catal. B: Environ.* 199 (2016) 412–423.
- [5] Y. Chen, H. Zhao, B. Liu, H.Q. Yang, Charge separation between wurtzite ZnO polar {001} surfaces and their enhanced photocatalytic activity, *Appl. Catal. B: Environ.* 163 (2015) 189–197.
- [6] S. Khanchandani, S. Kundu, A. Patra, A.K. Ganguli, Band gap tuning of ZnO/In<sub>2</sub>S<sub>3</sub> core/shell nanorod arrays for enhanced visible-light-driven photocatalysis, *J. Phys. Chem. C* 117 (2013) 5558–5567.
- [7] A.B. Djurišić, X. Chen, Y.H. Leung, A.M.C. Ng, ZnO nanostructures: growth, properties and applications, *J. Mater. Chem.* 22 (2012) 6526–6535.
- [8] M. Samadi, M. Zirak, A. Naseri, E. Khorashadizade, A.Z. Moshfegh, Recent progress on doped ZnO nanostructures for visible-light photocatalysis, *Thin Solid Films* 605 (2016) 2–19.
- [9] Y. Wang, Q. Wang, X. Zhan, F. Wang, M. Safdar, J. He, Visible light driven type II heterostructures and their enhanced photocatalysis properties: a review, *Nanoscale* 5 (2013) 8326–8339.
- [10] S. Harish, M. Navaneethan, J. Archana, A. Silambarasan, S. Ponnusamy, C. Muthamizhchelvan, Y. Hayakawa, Controlled synthesis of organic ligand passivated ZnO nanostructures and their photocatalytic activity under visible light irradiation, *Dalton Trans.* 44 (2015) 10490–10498.
- [11] F.H. Zhao, X.Y. Li, J.G. Zheng, X.F. Yang, F.L. Zhao, K.S. Wong, J. Wang, W.J. Lin, M.M. Wu, Q. Su, ZnO pine-nanotree arrays grown from facile metal chemical corrosion and oxidation, *Chem. Mater.* 20 (2008) 1197–1199.
- [12] Y. Peng, Y. Wang, Q.-G. Chen, Q. Zhu, A.W. Xu, Stable yellow ZnO mesocrystals with efficient visible-light photocatalytic activity, *CrystEngComm* 16 (2014) 7906–7913.
- [13] M. Misra, P. Kapur, M.L. Singla, Surface plasmon quenched of near band edge emission and enhanced visible photocatalytic activity of Au@ZnO core-shell nanostructure, *Appl. Catal. B: Environ.* 150–151 (2014) 605–611.
- [14] S.A. Ansari, M.M. Khan, M.O. Ansari, J. Lee, M.H. Cho, Biogenic synthesis photocatalytic, and photoelectrochemical performance of Ag-ZnO nanocomposite, *J. Phys. Chem. C* 117 (2013) 27023–27030.
- [15] Y. Lu, Y. Lin, T. Xie, S. Shi, H. Fan, D. Wang, Enhancement of visible-light-driven photoresponse of Mn/ZnO system: photogenerated charge transfer properties and photocatalytic activity, *Nanoscale* 4 (2012) 6393–6400.
- [16] S. Liu, C. Li, J. Yu, Q. Xiang, Improved visible-light photocatalytic activity of porous carbon self-doped ZnO nanosheet-assembled flowers, *CrystEngComm* 13 (2011) 2533–2541.
- [17] C. Wu, Facile one-step synthesis of N-doped ZnO micropolyhedrons for efficient photocatalytic degradation of formaldehyde under visible-light irradiation, *Appl. Surf. Sci.* 319 (2014) 237–243.
- [18] B. Subash, B. Krishnakumar, M. Swaminathan, M. Shanthi, Highly efficient, solar active, and reusable photocatalyst: r-loaded Ag-ZnO for reactive red 120 dye degradation with synergistic effect and dye-sensitized mechanism, *Langmuir* 29 (2012) 939–949.
- [19] M.T. Qamar, M. Aslam, I.M.I. Ismail, N. Salah, A. Hameed, Synthesis characterization, and sunlight mediated photocatalytic activity of CuO coated ZnO for the removal of nitrophenols, *ACS Appl. Mater. Interfaces* 7 (2015) 8757–8769.
- [20] S. Khanchandani, P.K. Srivastava, S. Kumar, S. Ghosh, A.K. Ganguli, Band gap engineering of ZnO using core/shell morphology with environmentally benign Ag<sub>2</sub>S sensitizer for efficient light harvesting and enhanced visible-light photocatalysis, *Inorg. Chem.* 53 (2014) 8902–8912.
- [21] X. Guo, H. Zhu, Q. Li, Visible-light-driven photocatalytic properties of ZnO/ZnFe<sub>2</sub>O<sub>4</sub> core/shell nanocable arrays, *Appl. Catal. B: Environ.* 160–161 (2014) 408–414.
- [22] L. Liu, Y. Qi, J. Lu, S. Lin, W. An, Y. Liang, W. Cui, A stable Ag<sub>3</sub>PO<sub>4</sub>@g-C<sub>3</sub>N<sub>4</sub> hybrid core@shell composite with enhanced visible light photocatalytic degradation, *Appl. Catal. B: Environ.* 183 (2016) 133–141.
- [23] L. Liu, L. Ding, Y. Liu, W. An, S. Lin, Y. Liang, W. Cui, A stable Ag<sub>3</sub>PO<sub>4</sub>@PANI core@shell hybrid: Enrichment photocatalytic degradation with π-π conjugation, *Appl. Catal. B: Environ.* 201 (2017) 92–104.
- [24] Y. Wang, R. Shi, J. Lin, Y. Zhu, Enhancement of photocurrent and photocatalytic activity of ZnO hybridized with graphite-like C<sub>3</sub>N<sub>4</sub>, *Energy Environ. Sci.* 4 (2011) 2922–2929.
- [25] Y.-P. Zhu, M. Li, Y.-L. Liu, T.-Z. Ren, Z.-Y. Yuan, Carbon-doped ZnO hybridized homogeneously with graphitic carbon nitride nanocomposites for photocatalysis, *J. Phys. Chem. C* 118 (2014) 10963–10971.
- [26] Y. He, Y. Wang, L. Zhang, B. Teng, M. Fan, High-efficiency conversion of CO<sub>2</sub> to fuel over ZnO/g-C<sub>3</sub>N<sub>4</sub> photocatalyst, *Appl. Catal. B: Environ.* 168–169 (2015) 1–8.
- [27] H. Moussa, E. Girot, K. Mozet, H. Alem, G. Medjahdi, R. Schneider, ZnO rods/reduced graphene oxide composites prepared via a solvothermal reaction for efficient sunlight-driven photocatalysis, *Appl. Catal. B: Environ.* 185 (2016) 11–21.
- [28] S. Xu, L. Fu, T.S.H. Pham, A. Yu, F. Han, L. Chen, Preparation of ZnO flower/reduced graphene oxide composite with enhanced photocatalytic performance under sunlight, *Ceram. Int.* 41 (2015) 4007–4013.
- [29] H. Zhang, R. Zong, Y. Zhu, Photocorrosion inhibition and photoactivity enhancement for zinc oxide via hybridization with monolayer polyaniline, *J. Phys. Chem. C* 113 (2009) 4605–4611.
- [30] R. Qiu, D. Zhang, Y. Mo, L. Song, E. Brewer, X. Huang, Y. Xiong, Photocatalytic activity of polymer-modified ZnO under visible light irradiation, *J. Hazard. Mater.* 156 (2008) 80–85.
- [31] Q. Luo, X. Li, X. Li, D. Wang, J. An, X. Li, Visible light photocatalytic activity of TiO<sub>2</sub> nanoparticles modified by pre-oxidized polyacrylonitrile, *Catal. Commun.* 26 (2012) 239–243.
- [32] D. Wang, Y. Duan, Q. Luo, X. Li, L. Bao, Visible light photocatalytic activities of plasmonic Ag/AgBr particles synthesized by a double jet method, *Desalination* 270 (2011) 174–180.
- [33] X. Li, R. Zheng, Q. Luo, D. Wang, J. An, R. Yin, Y. Liu, D. Wu, X. Han, Cyclized polyacrylonitrile modified Ag<sub>3</sub>PO<sub>4</sub> photocatalysts with enhanced photocatalytic activity under visible-light irradiation, *Appl. Surf. Sci.* 199 (2015) 96–104.
- [34] D. Wang, H. Sun, Q. Luo, X. Yang, R. Yin, An efficient visible-light photocatalyst prepared from g-C<sub>3</sub>N<sub>4</sub> and polyvinyl chloride, *Appl. Catal. B: Environ.* 156–157 (2014) 323–330.
- [35] H.K. Shin, M. Park, P.H. Kang, H.-S. Choi, S.-J. Park, Preparation and characterization of polyacrylonitrile-based carbon fibers produced by electron beam irradiation pretreatment, *J. Ind. Eng. Chem.* 20 (2014) 3789–3792.
- [36] E.D. Holt, N. Shaham-Waldmann, Y. Paz, Heat-treated polyacrylonitrile nanofibers: a new material for efficient photo-assisted reduction of Cr (VI), *J. Photochem. Photobiol. A* 257 (2013) 26–33.
- [37] C.-K. Liu, Y. Feng, H.-J. He, J. Zhang, R.-J. Sun, M.-Y. Chen, Effect of carbonization temperature on properties of aligned electrospun polyacrylonitrile carbon nanofibers, *Mater. Des.* 85 (2015) 483–486.
- [38] K.I. Lee, J. Li, B. Fei, J.H. Xin, Mechanism study of heat stabilization of polyacrylonitrile nanofibers against alkaline hydrolysis, *Polym. Degrad. Stab.* 105 (2014) 80–85.
- [39] T.J. Xue, M.A. McKinney, C.A. Wilkie, The thermal degradation of polyacrylonitrile, *Polym. Degrad. Stab.* 58 (1997) 193–202.
- [40] R. Wang, Synthesis of ZnO@ZnS–Bi<sub>2</sub>S<sub>3</sub> core–shell nanorod grown on reduced graphene oxide sheets and its enhanced photocatalytic performance, *J. Mater. Chem. 2* (2014) 8304–8313.
- [41] W. Yu, D. Xu, T. Peng, Enhanced photocatalytic Activity of g-C<sub>3</sub>N<sub>4</sub> for selective CO<sub>2</sub> reduction to CH<sub>3</sub>O via facile coupling of ZnO: a direct Z-scheme mechanism, *J. Mater. Chem. A* 3 (2015) 19936–19947.
- [42] A. Kumar, S. Baruah, B. Tonda, V. Kumar, Cost-effective and eco-friendly synthesis of novel and stable N-doped ZnO/g-C<sub>3</sub>N<sub>4</sub> core–shell nanoplates with excellent visible-light responsive photocatalysis, *Nanoscale* 6 (2014) 4830–4842.
- [43] D.E. Motaung, G.H. Mhlongo, S.S. Nkosi, G.F. Malgas, B.W. Mwakikunga, E. Coetsee, H.C. Swart, H.M. Abdallah, T. Moyo, S.S. Ray, Shape-selective dependence of room temperature ferromagnetism induced by hierarchical ZnO nanostructures, *ACS Appl. Mater. Interfaces* 6 (2014) 8981–8995.
- [44] V.L. Chandraboss, J. Kamalakkannan, S. Prabha, S. Senthivelan, An efficient removal of methyl violet from aqueous solution by an AC-Bi/ZnO nanocomposite material, *RSC Adv.* 5 (2015) 25857–25869.
- [45] Y. Hong, C. Tian, B. Jiang, A. Wu, Q. Zhang, G. Tian, H. Fu, Facile synthesis of sheet-like ZnO assembly composed of small ZnO particles for highly efficient photocatalysis, *J. Mater. Chem. A* 1 (2013) 5700–5708.
- [46] S. Park, T. Ikegami, K. Ebihara, Effects of substrate temperature on the properties of Ga-doped ZnO by pulsed laser deposition, *Thin Solid Films* 513 (2006) 90–94.
- [47] Z. Pei, L. Ding, J. Hu, S. Weng, Z. Zheng, M. Huang, P. Liu, Defect and its dominance in ZnO films: a new insight into the role of defect over photocatalytic activity, *Appl. Catal. B: Environ.* 142–143 (2013) 736–743.

[48] X. Pan, Y. Xu, Fast and spontaneous reduction of gold ions over oxygen-vacancy-rich TiO<sub>2</sub>: A novel strategy to design defect-based composite photocatalyst, *Appl. Catal. A: Gen.* 459 (2013) 34–40.

[49] Y. Lv, Y. Liu, Y. Zhu, Y. Zhu, Surface oxygen vacancy induced photocatalytic performance enhancement of a BiPO<sub>4</sub> nanorod, *J. Mater. Chem. A* 2 (2014) 1174–1182.

[50] Y. Zhang, Z. Chen, S. Liu, Y. Xu, Size effect induced activity enhancement and anti-photocorrosion of reduced graphene oxide/ZnO composites for degradation of organic dyes and reduction of Cr(VI) in water, *Appl. Catal. B: Environ.* 140–141 (2013) 598–607.

[51] Y. Liang, S. Lin, L. Liu, J. Hu, W. Cui, Oil-in-water self-assembled Ag@AgCl QDs sensitized Bi<sub>2</sub>WO<sub>6</sub>: Enhanced photocatalytic degradation under visible light irradiation, *Appl. Catal. B: Environ.* 164 (2015) 192–203.

[52] E.D. Owen, H.S.M. Al-Moh'd, Polyene sequences in iodinated polyisoprene, *Polymer* 38 (1997) 3533–3538.

[53] T. Xu, Y. Cai, K.E. O'Shea, Adsorption and photocatalyzed oxidation of methylated arsenic species in TiO<sub>2</sub> suspensions, *Environ. Sci. Technol.* 41 (2007) 5471–5477.

[54] I. Kwiatkowski, ZnO nanorods covered with a TiO<sub>2</sub> layer: simple sol-gel preparation, and optical, photocatalytic and photoelectrochemical properties, *J. Mater. Chem. 3* (2015) 12748–12760.

[55] J. Li, M. Zhou, Z. Ye, H. Wang, C. Ma, P. Huo, Y. Yan, Enhanced photocatalytic activity of g-C<sub>3</sub>N<sub>4</sub>–ZnO/HNT composite heterostructure photocatalysts for degradation of tetracycline under visible light irradiation, *RSC Adv.* 5 (2015) 91177–91189.

[56] R. Ye, H.B. Fang, Y.-Z. Zheng, N. Li, Y. Wang, X. Tao, Fabrication of CoTiO<sub>3</sub>/g-C<sub>3</sub>N<sub>4</sub> hybrid photocatalysts with enhanced H<sub>2</sub> evolution: -scheme photocatalytic mechanism insight, *ACS Appl. Mater. Interfaces* 8 (2016) 13879–13889.

[57] Y. Hong, Y. Jiang, C. Li, W. Fan, X. Yan, M. Yan, W. Shi, In-situ synthesis of direct solid-state Z-scheme V<sub>2</sub>O<sub>5</sub>/g-C<sub>3</sub>N<sub>4</sub> heterojunctions with enhanced visible light efficiency in photocatalytic degradation of pollutants, *Appl. Catal. B: Environ.* 180 (2016) 663–673.

[58] K. Sekizawa, K. Maeda, K. Domen, K. Koike, O. Ishitani, Artificial Z-scheme constructed with a supramolecular metal complex and semiconductor for the photocatalytic reduction of CO<sub>2</sub>, *J. Am. Chem. Soc.* 135 (2013) 4596–4599.